Earth's Future

Supporting Information for

What does global land climate look like at 2 degrees warming?

Taejin Park[1,2,*], Hirofumi Hashimoto[1,3], Weile Wang[1], Bridget Thrasher[4], Andrew R. Michaelis[1], Tsengdar Lee[5], Ian G. Brosnan[1], Ramakrishna R. Nemani[1,2]

[1]NASA Ames Research Center, CA, United States
[2]Bay Area Environmental Research Institute, CA, United States
[3]California State University Monterey Bay, CA, United States
[4]Climate Analytics Group, CO, United States
[5]NASA Headquarters, Washington DC, United States

Contents of this file

Text S1

Supplementary Methods

Comparison between CMIP5- and CMIP6-based crossing year detection

We additionally examine how the +2 °C crossing year from CMIP6 differs from the one from CMIP5 (21 GCMs, Table S1). We detect MME- and individual GCM- based +2 °C crossing years by following the approach described in Section 2.2. Due to the absence of *tas* in CMIP5, we derive the value from the average of maximum and minimum near-surface air temperature (WMO, 2018). Our extra-comparison analysis against CMIP5 shows that CMIP6 models tend to reach +2 °C crossing year earlier than those of CMIP5 models (RCP4.5=2046, RCP8.5=2042) (Figure S1). This discrepancy indicates CMIP6 models have a more rapid increase in temperature than those in CMIP5 due to a higher equilibrium climate sensitivity in the latest GCMs caused primarily by stronger positive cloud feedbacks (Zelinka et al., 2020).

Description of moisture and fire-behavior indices in FWI

Fine Fuel Moisture Code (FFMC): The FFMC is a numeric rating of the moisture content of litter and other cured fine fuels occupying the first fuel bed layers (surface layer, 1-2 cm deep). This code is an indicator of the relative ease of ignition and the flammability of fine fuel. The FFMC rating is defined in the range from 2 to 101, as suggested by Van Wagner. The typical FFMC default startup value is, by convention, equal to 85. The reanalysis dataset considered here is obtained as a single model run starting on 1st January 1950. However, the first year is discarded to ignore the effects of the initial model spin-up and no seasonal start-stopping rule is implemented (same applies to the other indices).

Duff Moisture Code (DMC): The DMC is a numeric rating of the average moisture content of loosely compacted organic layers of moderate depth (duff layer, 5–10 cm). This code gives an indication of fuel consumption in moderate duff layers and medium-size woody material. DMC is characterized by a medium-term response (about 10–12 days) to weather variations. The rating is defined in the range from zero to infinity, however, the default startup value is conventionally set equal to 6.

Drought Code (DC): The DC is a numeric rating of the average moisture content of deep, compact organic layers (deep duff layer, 1–20 cm). This code is a useful indicator of seasonal drought effects on forest fuels and the amount of smoldering in deep duff layers and large logs. DC has a long-term response (about 50 days) to weather variations. The rating is defined in the range from zero to infinity, with a default startup value equal to 15.

Initial Spread Index (ISI): The ISI is a numeric rating that measures the rate at which a fire would spread in its early stages shortly after ignition. It combines the effects of wind and the FFMC on rate of spread without the influence of variable quantities of fuel. ISI is defined in the range from zero to infinity.

Build Up Index (BUI): The BUI is a numeric rating of the total amount of fuel available for combustion. It is a weighted combination of the DMC and DC and defined in the range from zero to infinity.

Quantification of spatial variations in key climate variables

The 21 Giorgi regions (Figure 1) is less effective in highlighting the merits of the downscaled climate projections. Therefore, to quantify the additional spatial variations the NEX-GDDP data provide on top of the original CMIP6 GCMs, we further compute the spatial coefficient of variations (CV, Equation 1) of NEX-GDDP CMIP6 climate variables at varying spatial resolutions. The CV is computed as below:

$$CV = 100 \times \frac{\sigma}{\mu} = 100 \times \frac{\sqrt{\frac{\sum(x_{i,j} - \frac{\sum x_{i,j}}{N})^2}{N}}}{\frac{\sum x_{i,j}}{N}} \quad \text{Eq.1}$$

where, μ and σ are mean and standard deviation of values (x) at pixels (i, j) within a given spatial resolution. N is total number of pixels. We compute the spatial CVs at varying spatial resolutions ranging from 0.25°×0.25° to 2.0°×2.0°. Note that we present only outcomes at a 1.5°×1.5° spatial resolution as each GCM has varying spatial resolution. As defined, this measure has lower/higher values over areas where homogeneous/heterogeneous changes are projected. It thus helps identify regions where the downscaled climate variables are more advantageous than the original GCM outputs in revealing the spatial patterns of climate changes.

Supplementary Results

Spatial variations captured from NEX-GDDP

The NEX-GDDP data (0.25°×0.25°) typically provides 16 to 64 times finer spatial information compared to the nominal CMIP6 GCM projections (1°~2° spatial resolution). Spatial variations captured in the downscaled data generally increase as a function of the nominal GCM's spatial resolution (Figures S10,11). For instance, spatial CV of precipitation increases by 8.2 % for every 1° nominal GCM's spatial resolution increase (Figure S11). Another noteworthy point is that the spatial CVs of each climate variable significantly differ and clearly suggest how heterogeneous changes are projected to occur in the 2040s. For instance, temperature, downwelling longwave radiation, and $sWBGT_{P95}$ show much lower CV globally compared to other climate variables. This difference indicates a widespread and homogeneous increase in temperature, downwelling longwave radiation, and $sWBGT_{P95}$, while changes in other climate variables are projected to be spatially heterogeneous.

For the spatial pattern of CV, here we mainly present the results at a 1.5° nominal spatial resolution for the sake of brevity (Figure S10). We generally see high CV values along boundaries between regions where a climate variable changes in opposite directions. For instance, a significant increase in precipitation over central Africa is obvious while the northern and southern African regions are projected to be stable or slightly decreasing (Figure 4b). Spatial variability of the changes is high especially over the boundaries of the contrasting precipitation changes (see Figure S10b). The spatial variability of the changes differs by climate variables. Our analysis reveals that the NEX-GDDP product can capture variation (coefficient of variation = standard deviation / mean) with-in pixel at 1.5 degree by $1.4^{2.2}_{0.9}$ %, $13.7^{28.6}_{7.3}$ %, $13.0^{27.6}_{6.9}$%, $7.6^{16.7}_{4.3}$ %, $2.5^{4.0}_{1.5}$%, and $13.4^{30.0}_{7.5}$ % for temperature, precipitation, relative humidity, downward short- and longwave radiations, and wind speed, respectively (Median, 25th and 75th percentiles are presented). We also find that about $2.3^{3.8}_{1.4}$% and $14.6^{30.7}_{7.9}$% of with-in pixel spatial variation in $sWBGT_{P95}$ and FWI_{P95} can be further captured in the NEX-GDDP data.

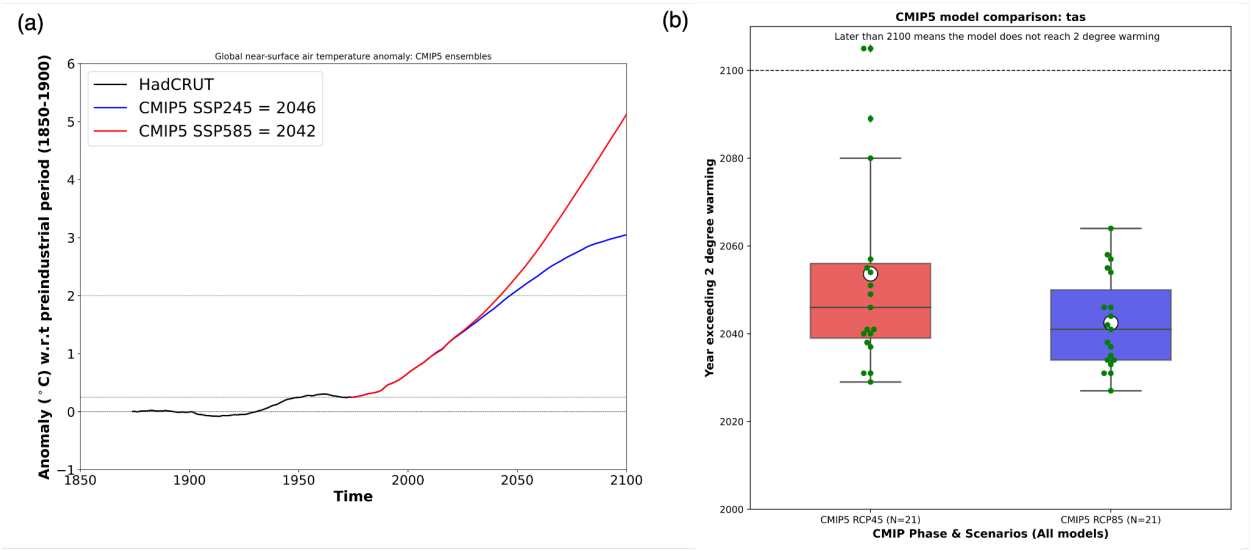

Figure S1. *(a) Time series of running 30-year average global mean near-surface air temperature of CMIP5 (blue: RCP4.5, red: RCP8.5) multi-model ensemble median. Green horizontal line shows 2 °C warming with respect to a baseline period (1950–1979) and detected crossing years are shown in the legend box. (b) Distribution of year exceeding 2 °C degree warming across CMIP5 (RCP4.5 & RCP8.5) GCMs under different scenarios. Each green dot represents individual GCMs of CMIP5. Note that dots greater than 2100 mean that the models do not project +2 °C warming until the end of 21st century.*

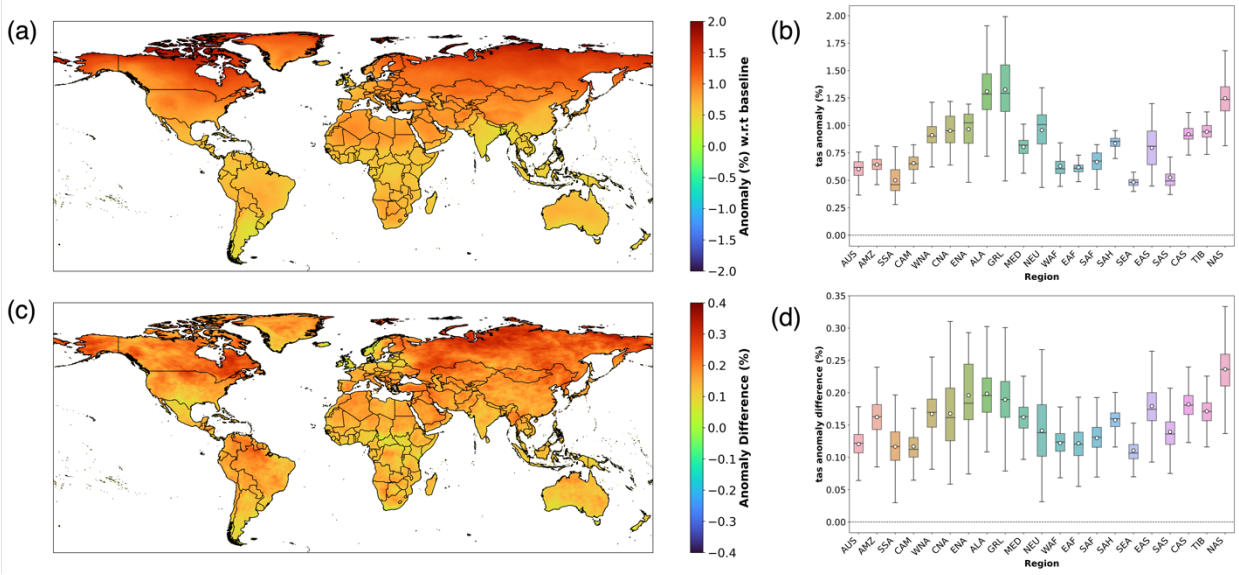

Figure S2. *(a) Spatial pattern of relative changes in the multimodel ensemble median (MME) of near surface air temperature (SSP2-4.5) in the 2040s with respect to the baseline period (1950-1979). (b) Regional summary of relative changes in the near-surface air temperature (SSP2-4.5) shown in (a). (c) Spatial pattern of differences between the computed relative changes in SSP2-4.5 and SSP5-8.5. (d) Regional summary of differences between the computed relative changes in SSP2-4.5 and SSP5-8.5 shown in (c). The box stretches from the 25th percentile to the 75th percentile of target regional data. The median and mean values are shown as a solid line and a hollow dot, respectively.*

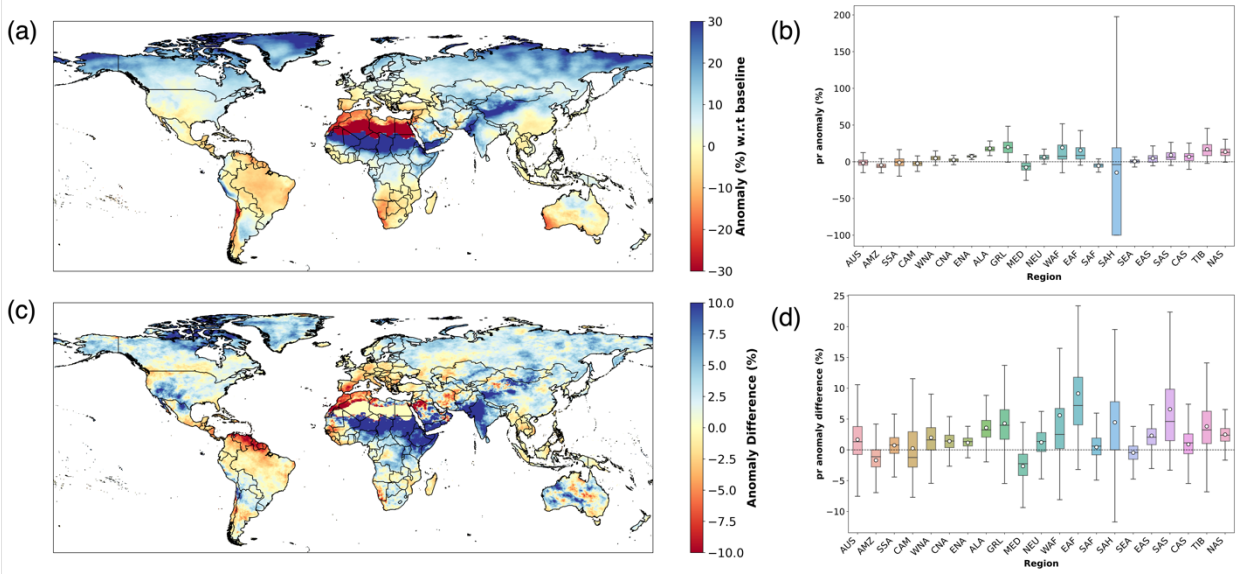

Figure S3. *Same as Figure S2 but for precipitation (pr).*

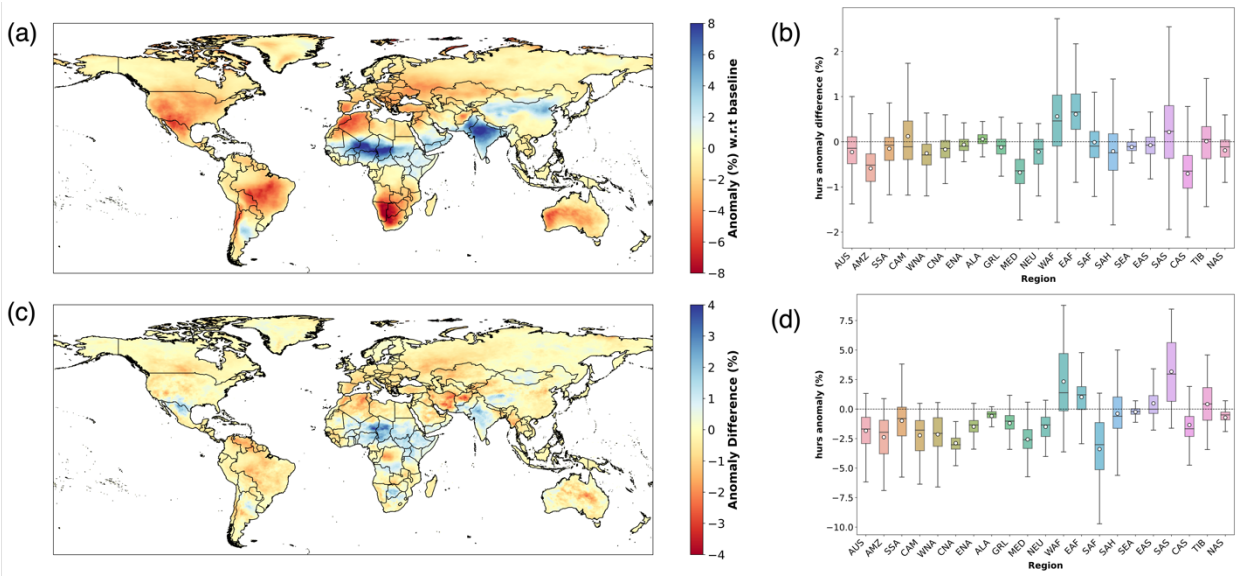

Figure S4. *Same as Figure S2 but for near-surface relative humidity (hurs).*

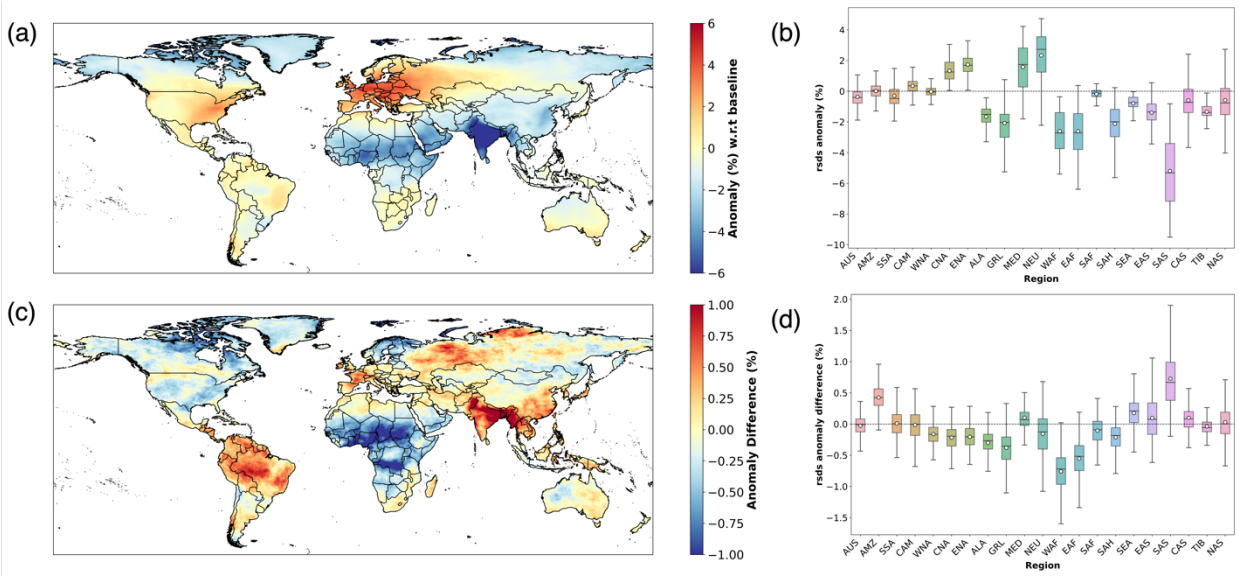

Figure S5. *Same as Figure S2 but for surface downwelling shortwave radiation (rsds).*

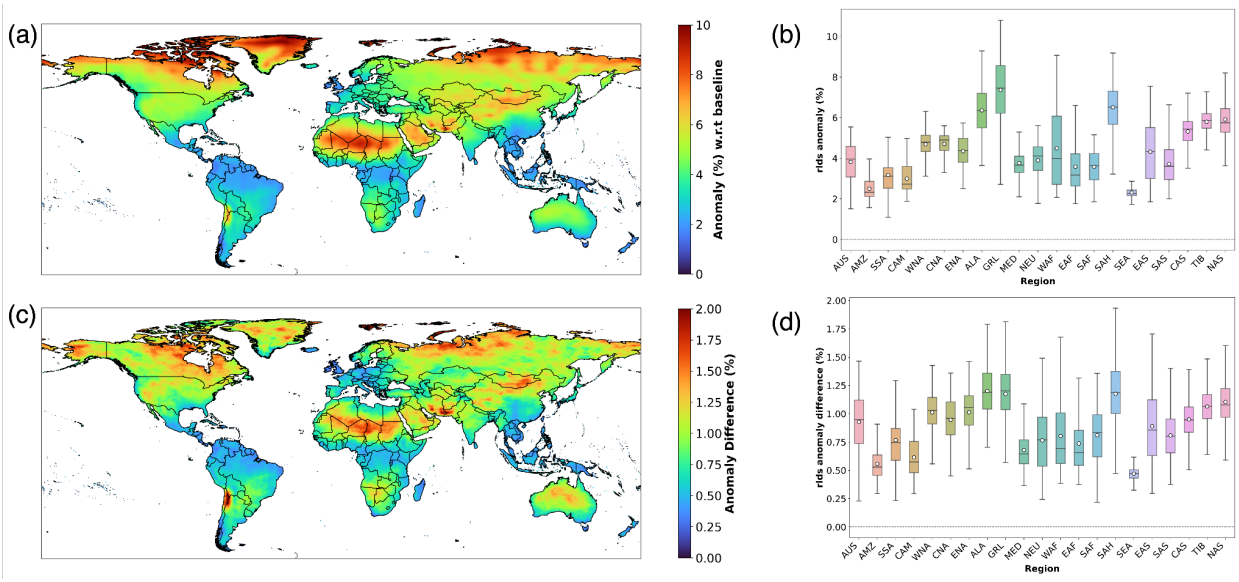

Figure S6. *Same as Figure S2 but for surface downwelling longwave radiation (rlds).*

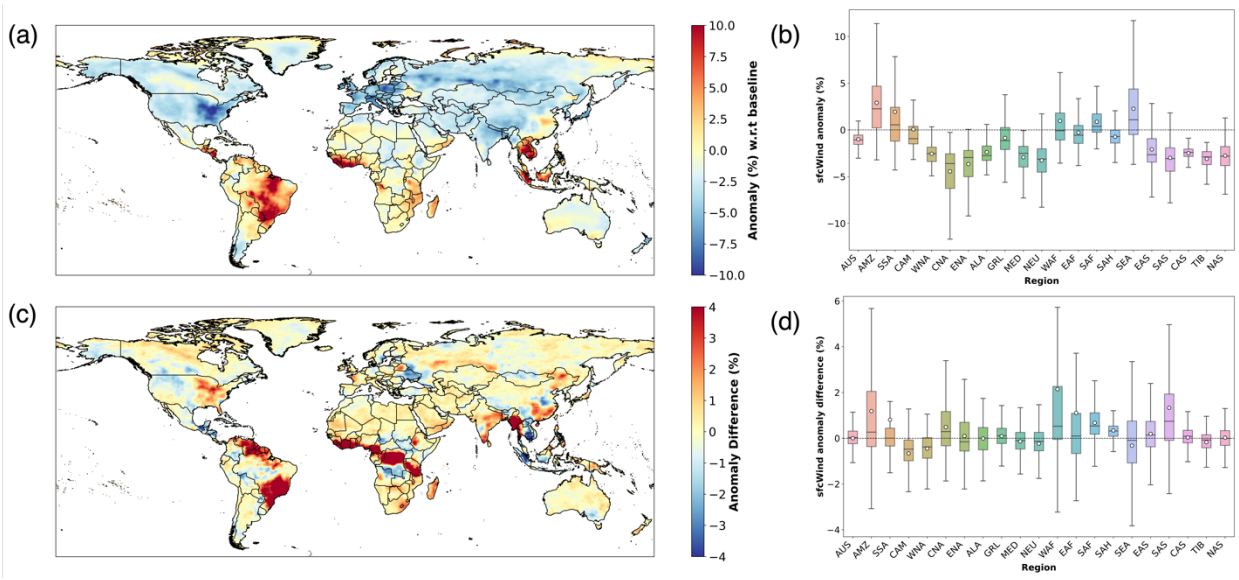

145

146 ***Figure S7.*** *Same as Figure S2 but for near-surface wind speed (sfcWind).*

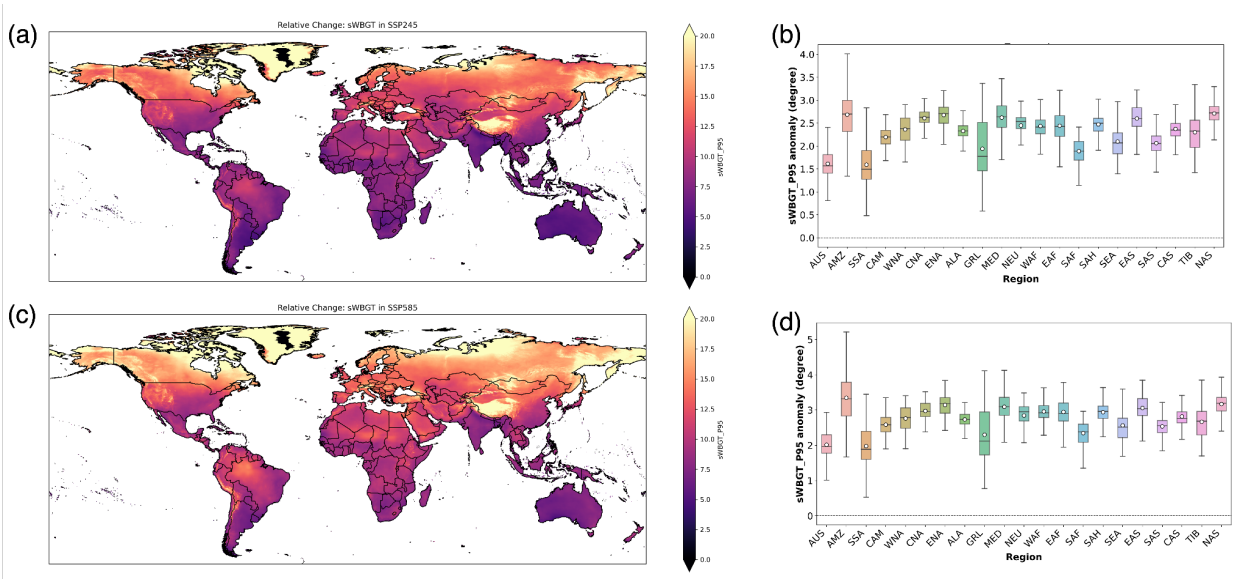

Figure S8. *Same as Figure S2 but for wet-bulb global temperature (sWBGT$_{P95}$).*

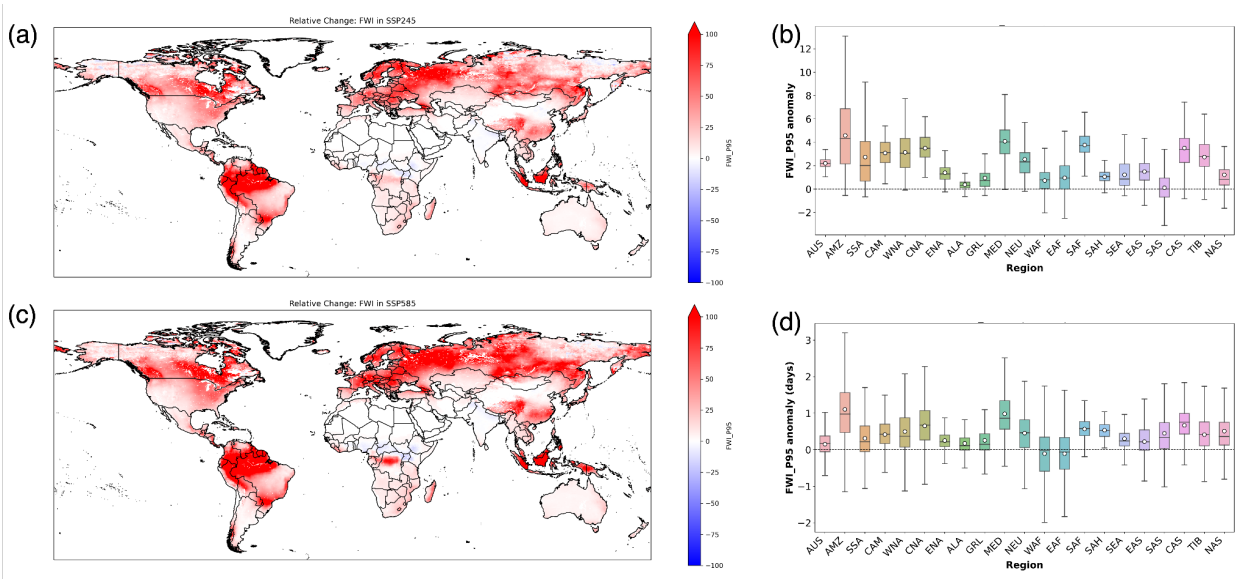

Figure S9. *Same as Figure S2 but for fire weather index (FWI_{P95}).*

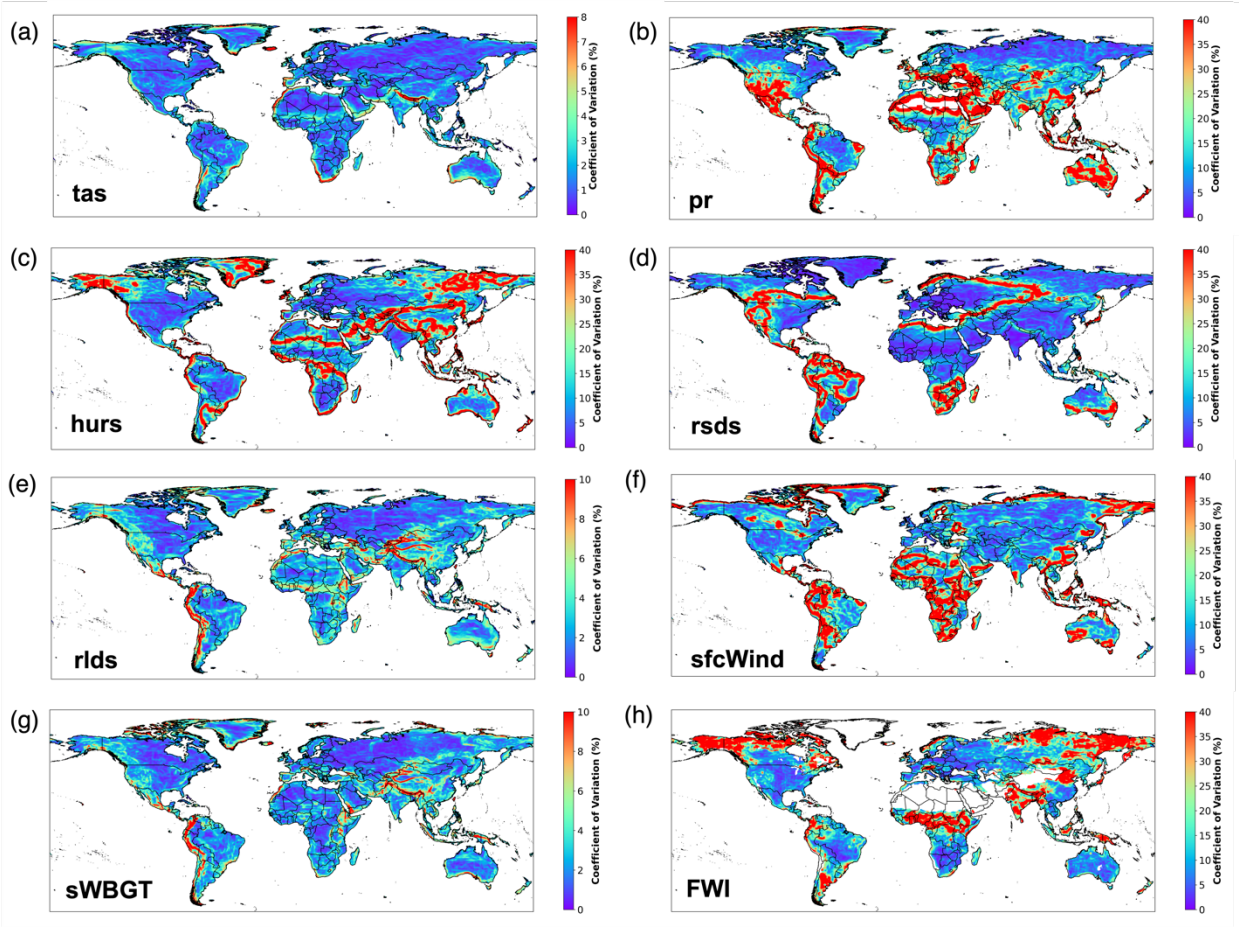

Figure S10. *Spatial pattern of spatial coefficient of variation (CV) in NEX-GDDP CMIP6 data at a 1.5°×1.5° spatial resolution: (a) mean near-surface air temperature (tas), (b) precipitation (pr), (c) near-surface relative humidity (hurs), (d) surface downwelling shortwave radiation (rsds), (e) surface downwelling longwave radiation longwave (rlds), (f) near-surface wind speed (sfcWind), (g) wet-bulb global temperature (sWBGT), and (h) fire weather index (FWI).*

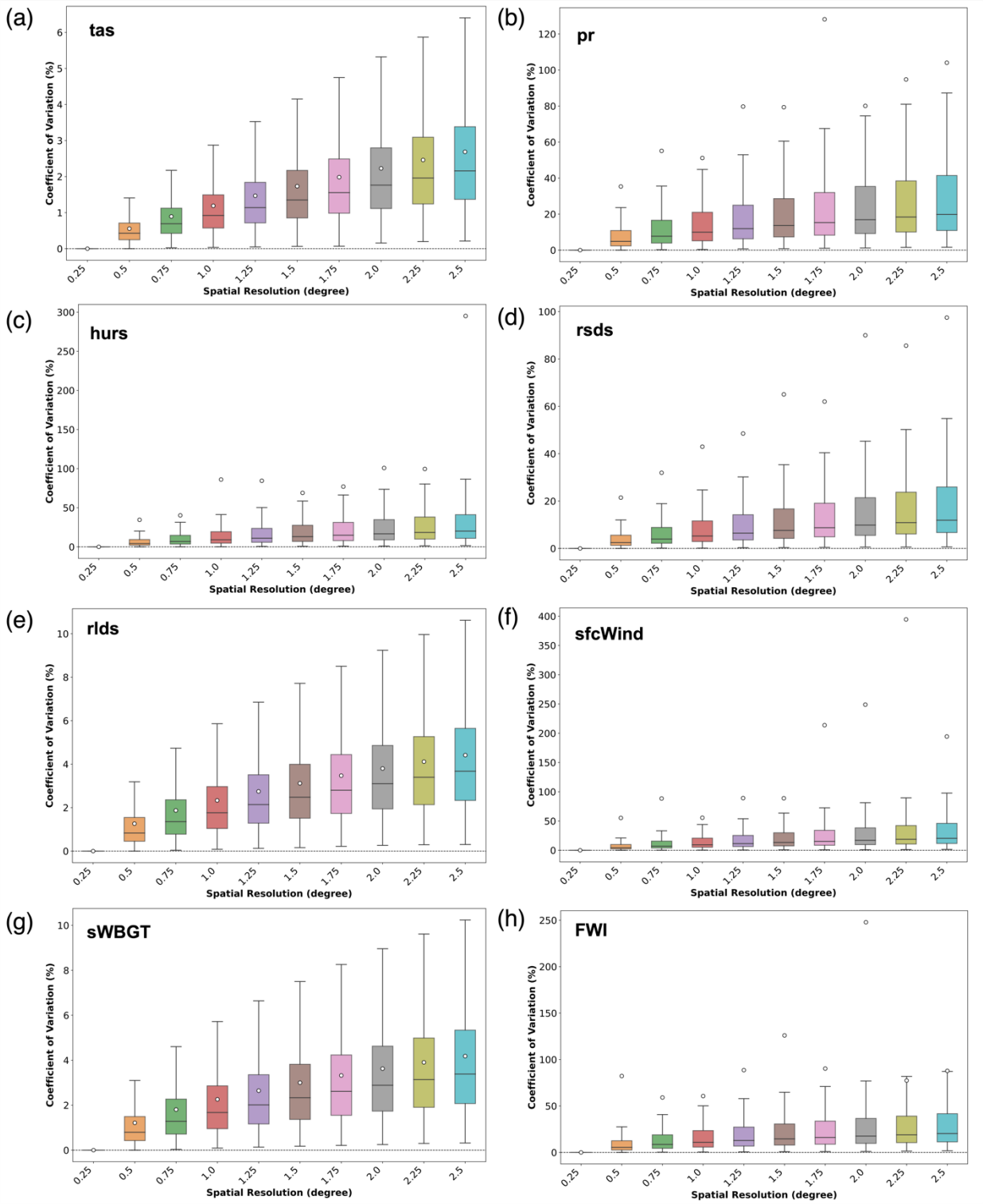

Figure S11. *Spatial coefficient of variation (CV) of NEX-GDDP CMIP6 data at given varying spatial resolutions: (a) mean near-surface air temperature (tas), (b) precipitation (pr), (c) near-surface relative humidity (hurs), (d) surface downwelling shortwave radiation (rsds), (e) surface*

downwelling longwave radiation longwave (rlds), (f) near-surface wind speed (sfcWind), (g) wet-bulb global temperature (sWBGT), and (h) fire weather index (FWI). The box stretches from the 25th percentile to the 75th percentile of target regional data. The median and mean values are shown as a solid line and a hollow dot, respectively.

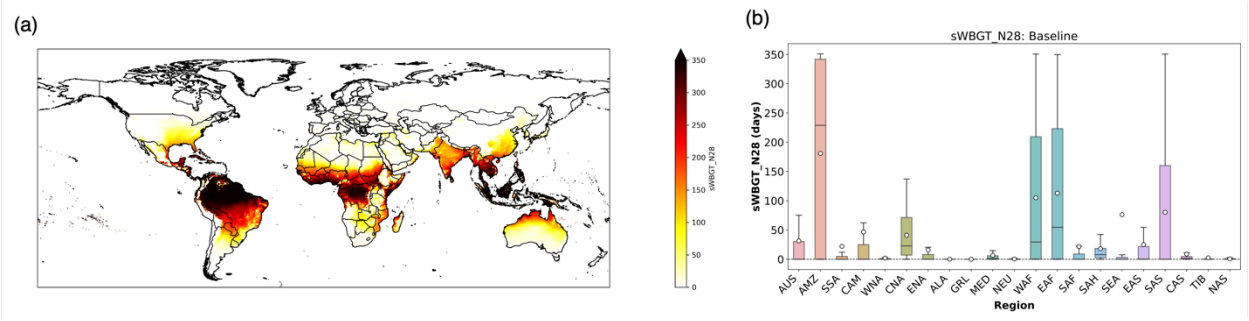

Figure S12. *(a) Spatial pattern of multimodel ensemble median (MME) of* $sWBGT_{N28}$ *during a baseline period (1950-1979). (b) Regional summary of the baseline* $sWBGT_{N28}$ *shown in (a). The box stretches from the 25th percentile to the 75th percentile of target regional data. The median and mean values are shown as a solid line and a hollow dot, respectively.*

176 **Table S1.** Description of NEX-GDDP CMIP5 data used in this study.

	GDDP-CMIP5
Model	Total 21 models: ACCESS1-0, bcc-csm1-1, BNU-ESM, CanESM2, CCSM4, CESM1-BGC, CNRM-CM5, CSIRO-Mk3-6-0, GFDL-CM3, GFDL-ESM2G, GFDL-ESM2M, inmcm4, IPSL-CM5A-LR, IPSL-CM5A-MR, MIROC-ESM, MIROC-ESM-CHEM, MIROC5, MPI-ESM-LR, MPI-ESM-MR, MRI-CGCM3, NorESM1-M
Simulation	Historical (1950-2004)
	rcp4.5 (2005-2100)
	rcp8.5 (2005-2100)
Variable	*tasmax*[1], *tasmin*[2]
Temporal Coverage	1950-01-01 to 2100-12-31
Temporal Resolution	Daily
Spatial Resolution	0.25° x 0.25°
[1]maximum near-surface air temperature (°C), [2]minimum near-surface air temperature (°C)	

177

178

Supplementary reference

World Meteorological Organization (WMO)., 2018. Guide to Climatological Practices. World Meteorological Organization.

Zelinka, M.D., Myers, T.A., McCoy, D.T., Po-Chedley, S., Caldwell, P.M., Ceppi, P., Klein, S.A., Taylor, K.E., 2020. Causes of higher climate sensitivity in CMIP6 models. Geophysical Research Letters 47, e2019GL085782.